A Great Earthquake Rupture Across a Rapidly Evolving Three-Plate Boundary
Kevin P. Furlong, *et al.*
Science **324**, 226 (2009);
DOI: 10.1126/science.1167476

vol. % of $(Mg_{0.8}Fe_{0.2})O$ contribute about equally to the overall possible seismic shear anisotropy as ~80 vol. % $MgSiO_3$ (Fig. 4). Because (Mg,Fe)O is a much weaker phase (*28*), it will accommodate most of the strain (*29*); it should, therefore, develop a much stronger texture than $(Mg,Fe)SiO_3$ (*13*). Thus, it is likely that LPO of (Mg,Fe)O dominates seismic anisotropy in the lower mantle. Strong partitioning of iron into ferropericlase, suggested by experiments (*19*, *30*), may favor even stronger anisotropy from (Mg,Fe)O. However, consensus on the partitioning behavior of iron under lower-mantle conditions has not been reached (*30*, *31*).

If LPO of ferropericlase dominates lower-mantle anisotropy, seismic anisotropy could also be present above the D″ discontinuity in regions where deformation is dominated by dislocation creep at very high strain levels (*6*, *9*). The rapid spreading of seismic receivers around the world will allow us to better quantify the depth distribution of anisotropy in the lower mantle.

References and Notes

1. M. Murakami, K. Hirose, K. Kawamura, N. Sata, Y. Ohishi, *Science* **304**, 855 (2004).
2. A. R. Oganov, S. Ono, *Nature* **430**, 445 (2004).
3. T. Lay, Q. Williams, E. J. Garnero, *Nature* **392**, 461 (1998).
4. E. J. Garnero, V. Maupin, T. Lay, M. J. Fouch, *Science* **306**, 259 (2004).
5. M. Panning, B. Romanowicz, *Science* **303**, 351 (2004).
6. A. K. McNamara, P. E. van Keken, S.-I. Karato, *Nature* **416**, 310 (2002).
7. J. Wookey, S. Stackhouse, J. M. Kendall, J. Brodholt, G. D. Price, *Nature* **438**, 1004 (2005).
8. J. M. Kendall, P. G. Silver, *Nature* **381**, 409 (1996).
9. H. R. Wenk, S. Speziale, A. K. McNamara, E. J. Garnero, *Earth Planet. Sci. Lett.* **245**, 302 (2006).
10. D. Yamazaki, S.-i. Karato, *Phys. Earth Planet. Inter.* **131**, 251 (2002).
11. B. B. Karki, R. M. Wentzcovitch, S. de Gironcoli, S. Baroni, *Science* **286**, 1705 (1999).
12. S. Merkel *et al.*, *Science* **316**, 1729 (2007).
13. R. M. Wentzcovitch, T. Tsuchiya, J. Tsuchiya, *Proc. Natl. Acad. Sci. U.S.A.* **103**, 543 (2006).
14. J. M. Jackson *et al.*, *J. Geophys. Res.* **111**, B09203 (2006).
15. S. D. Jacobsen *et al.*, *J. Geophys. Res.* **107**, 2037 (2002).
16. H. J. Reichmann, S. V. Sinogeikin, J. D. Bass, *Am. Mineral.* **93**, 1306 (2008).
17. S. V. Sinogeikin, J. D. Bass, *Phys Earth Planet. Inter.* **120**, 43 (2000).
18. C.-S. Zha, H.-k. Mao, R. J. Hemley, *Proc. Natl. Acad. Sci. U.S.A.* **97**, 13494 (2000).
19. J. Badro *et al.*, *Science* **300**, 789 (2003).
20. J. C. Crowhurst, J. M. Brown, A. F. Goncharov, S. D. Jacobsen, *Science* **319**, 451 (2008).
21. J.-F. Lin *et al.*, *Nature* **436**, 377 (2005).
22. S. Speziale *et al.*, *Proc. Natl. Acad. Sci. U.S.A.* **102**, 17918 (2005).
23. J.-F. Lin *et al.*, *Geophys. Res. Lett.* **33**, L22304 (2006).
24. Materials and methods are available as supporting material on *Science* online.
25. H. Keppler, I. Kantor, L. Dubrovinsky, *Am. Mineral.* **92**, 433 (2007).
26. T. Tsuchiya, K. Kawamura, *J. Chem. Phys.* **114**, 10086 (2001).
27. T. Tsuchiya, R. M. Wentzcovitch, C. R. S. da Silva, S. de Gironcoli, *Phys. Rev. Lett.* **96**, 198501 (2006).
28. S.-i. Karato, *Phys Earth Planet. Inter.* **55**, 234 (1989).
29. K. Madi, S. Forest, P. Cordier, M. Boussuge, *Earth Planet. Sci. Lett.* **237**, 223 (2005).
30. M. Murakami, K. Hirose, N. Sata, Y. Ohishi, *Geophys. Res. Lett.* **32**, L03304 (2005).
31. Y. Kobayashi *et al.*, *Geophys. Res. Lett.* **32**, L19301 (2005).
32. M. Murakami, Y. Ohishi, N. Hirao, K. Hirose, *Earth Planet. Sci. Lett.* **277**, 123 (2009).
33. J.-F. Lin *et al.*, *Science* **317**, 1740 (2007).

34. We thank J.-F. Lin, S. Jahn, T. Duffy, M. Koch-Müller, R. Jeanloz, K. Hartmann, and two anonymous reviewers for helpful comments and ideas on the project and the manuscript; A. Kurnosov for gas-loading at Bayerisches Geoinstitut, H. Wilhelm for assistance at the Diamond Light Source; and M. Gottschalk and T. Boffa Ballaran for single-crystal x-ray diffraction. E.J.G. acknowledges support from NSF grant EAR-0711401.

Supporting Online Material

www.sciencemag.org/cgi/content/full/324/5924/224/DC1
Materials and Methods
Figs. S1 to S5
Table S1
References

4 December 2008; accepted 16 February 2009
10.1126/science.1169365

A Great Earthquake Rupture Across a Rapidly Evolving Three-Plate Boundary

Kevin P. Furlong,[1]* Thorne Lay,[2] Charles J. Ammon[1]

On 1 April 2007 a great, tsunamigenic earthquake (moment magnitude 8.1) ruptured the Solomon Islands subduction zone at the triple junction where the Australia and Solomon Sea–Woodlark Basin plates simultaneously underthrust the Pacific plate with different slip directions. The associated abrupt change in slip direction during the great earthquake drove convergent anelastic deformation of the upper Pacific plate, which generated localized uplift in the forearc above the subducting Simbo fault, potentially amplifying local tsunami amplitude. Elastic deformation during the seismic cycle appears to be primarily accommodated by the overriding Pacific forearc. This earthquake demonstrates the seismogenic potential of extremely young subducting oceanic lithosphere, the ability of ruptures to traverse substantial geologic boundaries, and the consequences of complex coseismic slip for uplift and tsunamigenesis.

Great earthquakes typically involve sudden sliding between two tectonic plates, and the largest events are located in subduction zones where an oceanic plate thrusts into the mantle below an overriding plate. In a few locations, a boundary between two oceanic plates impinges on a subduction zone, causing both plates to descend beneath the overriding plate, but at different rates and directions. This is the situation that led to the great moment magnitude M_w 8.1 Solomon Islands earthquake of 1 April 2007 [8.47°S, 157.04°E, 20:39:58.7 UTC (*1*)], which ruptured the megathrust between the overriding Pacific plate (PaP) and the independently subducting Australia (AuP) and Solomon Sea–Woodlark Basin (SWP) plates (Fig. 1). The inferred rupture area along the San Cristobal and New Britain trenches, as indicated by aftershocks (*1*), patterns of uplift/subsidence (*2*–*4*), and preliminary rupture analysis (*5*, *6*), straddles the down-dip extension of the Simbo transform fault that separates the SWP from the AuP; thus, the earthquake ruptured across the SWP-AuP plate boundary. The rupture generated a large local tsunami, and about 50 lives were lost and more than 9000 people displaced.

Before the 2007 event, this triple junction region, where the three plates meet, had low seismic activity and no record of large interplate events (*7*); thus, pre-event seismicity, or other available geologic and tectonic data, provided limited constraint on the subduction zone geometry. The region above the down-dip extension of the Simbo Fault is a localized region of rapid Holocene uplift (*8*). The age of lithosphere currently subducting along the trench varies from ~0.5 to 3.5 million years old, and it has been speculated that such young, hot lithosphere will not produce large earthquakes. Here we describe the 2007 earthquake rupture to address how, before the earthquake, strain was distributed between the subducting and overriding plates.

Before ~0.5 million years ago (Ma), the easternmost segment of the Woodlark Basin spreading ridge was subducting beneath the western margin of the Solomon Islands (Fig. 1), and the ridge-trench triple junction migrated northwesterly at ~110 to 120 mm/year. The differences in plate subduction rates and directions produced a slab window, which today lies beneath the southern New Georgia Islands. The SWP subducts at 135 mm/year (N45°E), whereas the AuP subducts at 97 mm/year (N70°E) (*8*, *9*). The near-total cessation of spreading on the most trenchward section of the Woodlark Basin ridge at ~0.5 Ma (*8*, *9*) and the formation of the right-lateral

[1]Department of Geosciences, The Pennsylvania State University, State College, PA 16802 USA. [2]Department of Earth and Planetary Sciences, University of California, Santa Cruz, CA 95064, USA.

*To whom correspondence should be addressed. E-mail: kevin@geodyn.psu.edu

strike-slip Simbo transform fault caused the Ghizo lithospheric fragment (Fig. 1) to be transferred from the SWP to the AuP. The Simbo transform now accommodates ~60 mm/year plate motion between SWP and AuP, and the new triple junction formed by the Simbo transform and the trench migrates southeastward at ~110 mm/year (fig. S1).

Teleseismic body waves and short-arc Rayleigh waves (R1) were collected to characterize the mainshock rupture. Azimuthal variations of the R1 source time functions (STFs) (*10*) constrain the average rupture length and rupture velocity. Figure 2 shows the R1 STFs, which are narrow (~50 s) in the rupture direction and broad (~180 s) in the opposite direction (*11*). The systematic duration variation is consistent with unilateral rupture parallel to the trench axis with an average rupture speed of 2.5 ± 0.4 km/s. The STFs suggest a seismic moment of 2.5×10^{21} N·m (M_w = 8.2), somewhat larger than the global centroid-moment tensor (GCMT) estimate, which has an unusually large (37°) dip (*5*). A large aftershock is evident in the STFs ~7 min after the mainshock. This M_w = 6.6 event initiated ~200 km to the northwest of the mainshock hypocenter (7.17°S, 155.78°E, 20:47:31.3 UTC).

We computed finite-fault models for relatively uniform azimuthal distributions of teleseismic *P* and *SH* waves, using a least-squares inversion (*12*) with prescribed fault orientation, specified rupture velocity V_r, and variable subfault rake and source time function (*11*). Our preferred solution is for a fault strike of 305° ± 5°, dip of 25° ± 5°, and V_r = 2.5 ± 0.4 km/s (Fig. 3). The main effect of variations in rupture velocity is a simple stretching of the slip zone (fig. S3). The basic solution is stable with respect to changes in fault dip (fig. S4), strike (fig. S5) and data subsets (fig. S6).

The slip model shows two main patches of slip at shallow depth along strike, with a systematic 36° difference in rake between the patches (the near-epicentral patch has an average rake of 49 ± 11°, and the northwestern patch has a rake of 85 ± 15°). A third region of deeper slip with rake varying between values for the two shallow patches is located ~100 km from the hypocenter. The body waves also indicate predominantly unilateral rupture, with a total duration of about 100 s and seismic moment M_o = 1.87×10^{21} N·m (M_w = 8.1). The basic slip attributes are consistent with those indicated by rapid studies (*5*, *6*).

The distinct directions of coseismic slip in the major slip regions define separate domains of interseismic strain accumulation. The position of this transition on the slab interface (Fig. 4) is consistent with the expected down-dip extent of the Simbo fault if it developed ~0.5 Ma. The consistency between the shallow earthquake slip directions and current relative plate motions for the two plate pairs delineates the region of the subducted Ghizo fragment that has been transferred from the SWP to the AuP. The gradual transition in fault slip between AuP-PaP and SWP-PaP relative motion directions down-dip of the subducted Simbo fault suggests that the subducted slab is still at least partially connected in that region, leading to complexity in the strain accumulation and coseismic release.

The limited depth extent of rupture in the southeastern main rupture patch (AuP-PaP interaction) is compatible with the extreme youth of the subducted plate and the extent and location of the slab window that developed during ridge subduction before 0.5 Ma (Fig. 1). The relatively small coseismic slip along the megathrust near the subducted Simbo fault is enigmatic, particularly given the appreciable uplift associated with this earthquake (*2*–*4*) in the region and the similar patterns of Holocene uplift (*8*) above the subducted transform fault.

There are two end-member scenarios for interseismic and coseismic elastic strain accumulation and release in subduction zones. In the "slab deformation" model, all interseismic elastic deformation occurs within the subducting slab—i.e., there is no deformation of a rigid upper plate. Under this assumption, all coseismic recovery would involve displacement of the slab. In the "upper plate deformation" model, the overriding plate accumulates all of the interseismic deformation, and thus coseismic displacements all occur within the upper plate. This latter case would produce more surface uplift and potentially be more tsunamigenic than the former. Subduction

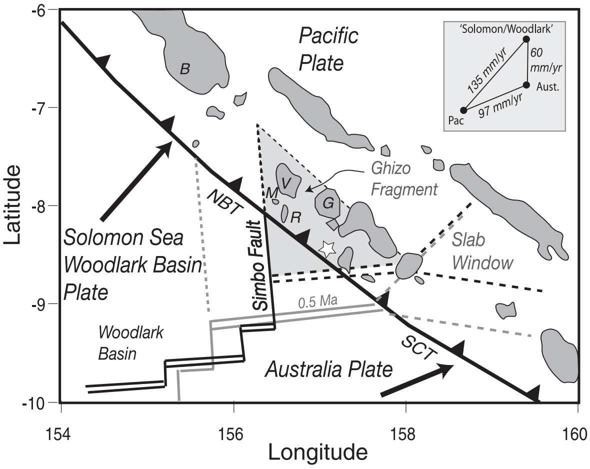

Fig. 1. Plate tectonic setting and recent tectonic evolution of the rupture area of the 1 April 2007, M_w 8.1 earthquake (epicenter shown by star). Plate boundary structures at ~0.5 Ma, including the incipient Simbo transform fault and the slab window produced by the subduction of the actively spreading Woodlark spreading ridge, are shown by gray lines. Black lines show present plate boundary structures. The shaded triangular region (Ghizo Fragment) maps the extent of subducted oceanic lithosphere that may have been transferred from the SWP to the AuP with the formation of the Simbo transform at ~0.5 Ma. Following Tregoning *et al.* (*17*), we consider the Woodlark Basin and Solomon Sea to comprise a single tectonic unit, the Solomon Sea–Woodlark Basin plate (SWP). The arrows show plate motions of the SWP and AuP relative to the PaP. The inset shows the plate motion velocity triangle in the earthquake rupture area. Locations labeled on map: SCT, San Cristobal trench; NBT, New Britain trench; B, Bougainville; M, Mbava; V, Vella Lavella; R, Ranongga; and G, Ghizo.

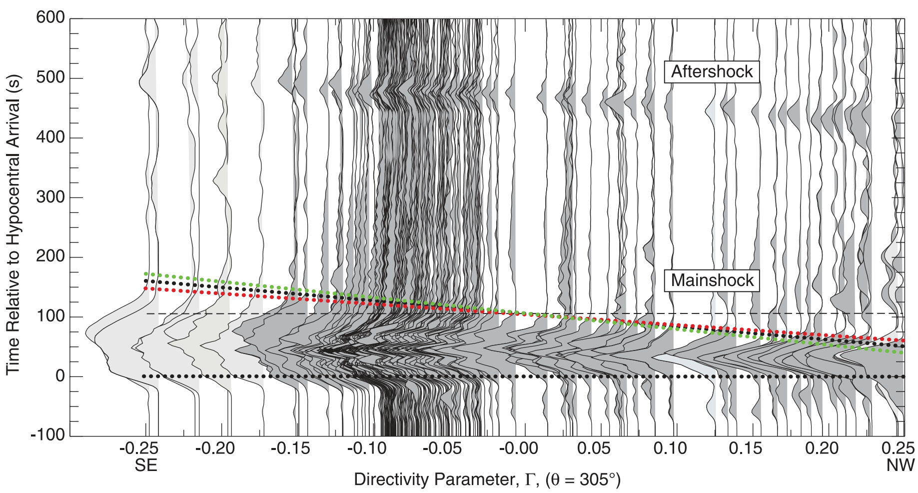

Fig. 2. R1 Rayleigh wave effective source time functions (STFs) plotted as a function of directivity parameter, Γ (*18*), assuming a rupture propagation azimuth of 305°. STFs along the direction of rupture (positive Γ) are shorter in duration, indicating predominantly unilateral rupture in the direction 305°. Fitting a line along the ends of the STFs, projected to limiting values of Γ (±0.25 s/km), allows one to estimate the minimum (52 s), maximum (182 s), and average (117 s) STF durations; each of these values has about ±10 s uncertainty due to scatter in the STFs. Lines indicate the onset, average, and end times of the STFs. STFs for a large aftershock about 7 min after the mainshock are apparent.

zone behavior likely falls somewhere between these two end-members, and normally seismologic observations are unable to distinguish in what domain a particular subduction plate boundary resides. If the Solomon subduction regime lies on the slab deformation end of the spectrum, then the coseismic slip behavior would require sympathetic or triggered slip on the subducted Simbo fault during the event and/or loading of the Simbo Fault. Neither appears to be the case (fig. S8).

Rather, the seismic cycle behavior of the Solomon subduction regime is consistent with that expected in the upper plate deformation model. Before the event, Global Positioning System displacements for the AuP, just to the south of the rupture region, indicated unimpeded motion of Australia with respect to the Pacific (*13*), implying little if any strain accumulation in the subducting Australia plate. Patterns of uplift associated with the earthquake (*2*, *3*) and the locations of maximum local tsunami run-up (*3*, *4*, *14*) are consistent with coseismic shortening in the upper plate in the transition zone between the two domains of interplate displacements (Fig. 4). The uplift, which may have been coseismic or rapid postseismic deformation, was observed on a suite of islands in the arc-trench region (*2*–*4*)—Ranongga, Mbava, and Vella Lavella—that overlie the location of the subducted Simbo transform and Simbo Ridge. Previously this near-trench uplift was attributed to uniform slip of 5 m over a narrow rectangular fault (*2*), but the more complex fault rupture pattern shown in Fig. 3 and in particular the relative minimum in fault slip right in the vicinity of the subducted Simbo transform suggest that an alternative mechanism, other than subduction of the bathymetry feature along the Simbo fault, may be needed to account for the uplift pattern.

Models of uplift driven by the observed pattern of coseismic slip show an increase in local uplift of >30% in that region (*15*). Similarly, the localization of maximum tsunami run-ups in that region (*3*, *4*) may represent the amplifying effects of the localized uplift (if coseismic) and/or reflect a constructive interference of waves produced by the two distinct patches of moment release. The lack of near-trench islands elsewhere along the margin hampers our ability to assess whether the uplift and tsunami run-ups observed on Ranongga are typical along the rupture zone. The existence of Ranongga (and associated islands) and the longer-term patterns of rapid uplift, >3 mm/year in the Holocene (*8*), for nearby islands implies that this region represents a relative maximum in near-trench uplift. As shown schematically in Fig. 4, under the assumption that this event represents an upper plate deformation case, our rupture model for the 2007 event indicates that this rapid uplift is a region of local along-arc convergence within the Pacific forearc between that overlying the southeastern rupture patch and the forearc overlying the northwestern rupture zone. This complex rupture pattern coupled with an upper plate–dominated deformation regime increases the seismic hazard in such areas.

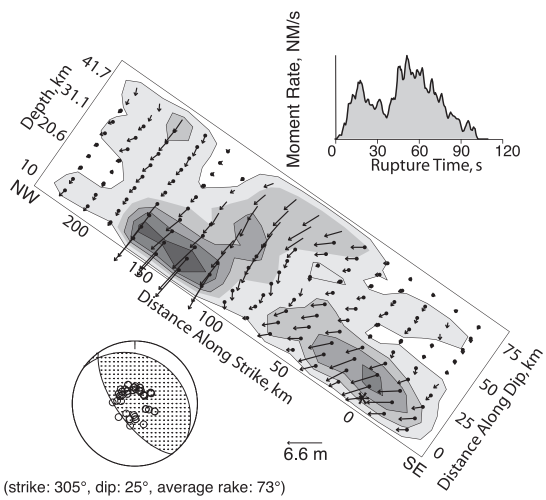

Fig. 3. Summary of the finite slip model for the mainshock obtained from inversion of *P* and *SH* waves. The model shows a source focal mechanism for the average fault orientation; the rupture surface with slip vectors indicating the sense of motion of the PaP relative to the SWP and AuP, with 1-m slip contour intervals; and the moment rate function, which indicates seismic energy release as a function of time. The seismic moment estimate, M_o, gives M_w = 8.1. The rupture velocity assumed in the inversion, V_r, is 2.5 km/s.

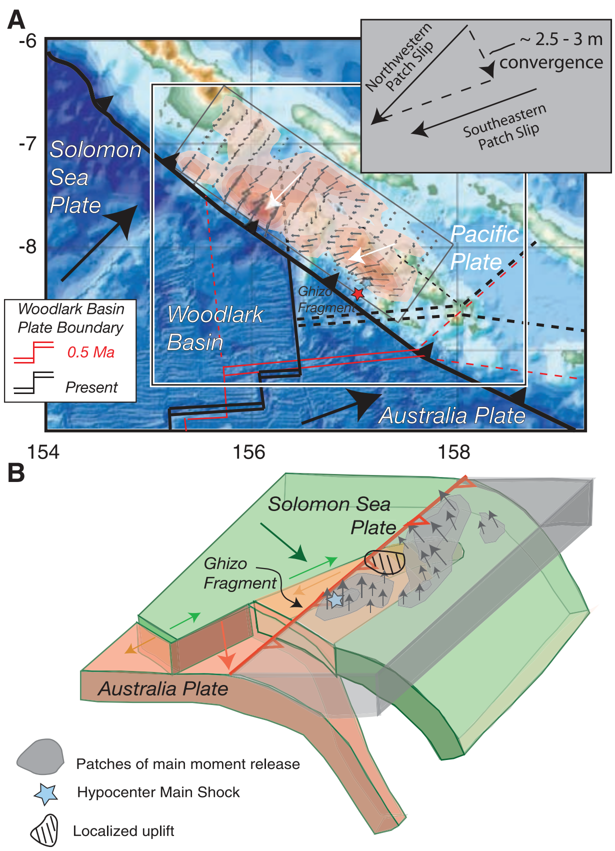

Fig. 4. Comparison of the earthquake slip model with the plate tectonic setting of the region. (**A**) Map view of the rupture model, which spans the region from the subducted (extinct) Woodlark spreading center to the initial location (at 0.5 Ma) of the Simbo transform triple junction. Inset shows kinematic relations between the slip along the two main patches of moment release, resulting in approximately 2.5 to 3.0 m of shortening within the overriding Pacific plate in the region of maximum observed uplift. (**B**) Three-dimensional view of rupture along the subduction interface. Coseismic slip on the southern patch of moment release suggests that region is fully connected to the Australia plate. Slip within the shallow northwestern patch suggests SWP affinities. The location of expected intraplate shortening during the coseismic slip within the Pacific plate is shown.

References and Notes

1. U. S. Geological Survey, http://earthquake.usgs.gov/eqcenter/eqinthenews/2007/us2007aqbk/ (2007).
2. F. W. Taylor *et al.*, *Nat. Geosci.* **1**, 253 (2008).
3. B. G. McAdoo *et al.*, *Eos Trans. AGU* **89**, 169 (2008).
4. H. M. Fritz, N. Kalligeris, *Geophys. Res. Lett.* **35**, L01607 (2008).
5. G. Ekström, M. Nettles, http://neic.usgs.gov/neis/eq_depot/2007/eq_070401_aqbk/neic_aqbk_hrv.html (2007).
6. C. Ji, http://earthquake.usgs.gov/eqcenter/eqinthenews/2007/us2007aqbk/finite_fault.php (2007).
7. T. Lay, H. Kanamori, *Phys. Earth Planet. Inter.* **21**, 283 (1980).
8. P. Mann, F. W. Taylor, M. B. Lagoe, A. Quarles, G. Burr, *Tectonophysics* **295**, 259 (1998).
9. K. A. W. Crook, B. Taylor, *Mar. Geophys. Lett.* **16**, 65 (1994).
10. C. J. Ammon, A. A. Velasco, T. Lay, *Geophys. Res. Lett.* **33**, L14314 10.1029/2006GL026303 (2006).
11. Additional details of the processing steps are available as supporting material on *Science* Online.
12. M. Kikuchi, H. Kanamori, www.eri.u-tokyo.ac.jp/ETAL/KIKUCHI/ (2003).
13. P. Tregoning, F. Tan, J. Gilliland, H. McQueen, K. Lambeck, *Geophys. Res. Lett.* **25**, 3627 (1998).
14. M. A. Fisher *et al.*, *Sci. Tsunami Hazards* **26**, 3 (2007).

15. Simple boundary element models using the average slip in the two main patches of the finite fault model produce a pattern of localized uplift in the region of convergence between the two slip domains that is >30% larger than at comparable distances from the trench along-strike. The lack of uplift and other slip observations away from the exposed islands preclude more detailed modeling at present.
16. A. M. Dziewonski, D. L. Anderson, *Phys. Earth Planet. Inter.* **25**, 297 (1981).
17. P. Tregoning *et al.*, *J. Geophys. Res.* **103**, 12181 (1998).
18. The directivity parameter, $\Gamma = \cos(\phi_{sta} - \phi_{rup})/c$, where ϕ_{sta} is the station azimuth, ϕ_{rup} is a unilateral rupture azimuth, and c is a reference phase velocity [c is chosen as 4.0 km/s, the phase velocity for 80-s-period Rayleigh waves for model PREM (*16*)].

19. The Incorporated Research Institutions for Seismology data management center provided the broadband seismic data. We thank C. Biryol and S. L. Beck for sharing a preprint manuscript and H. Kanamori for discussions about surface wave STFs and slip inversions. This work was supported in part by NSF under grant EAR0635570 (T.L.). We thank three anonymous reviewers for comments on the manuscript.

Supporting Online Material
www.sciencemag.org/cgi/content/full/324/5924/226/DC1
Methods
Figs. S1 to S11
Table S1
References

21 October 2008; accepted 26 February 2009
10.1126/science.1167476

Curved Plasma Channel Generation Using Ultraintense Airy Beams

Pavel Polynkin,[1]* Miroslav Kolesik,[1] Jerome V. Moloney,[1,2] Georgios A. Siviloglou,[3] Demetrios N. Christodoulides[3]

Plasma channel generation (or filamentation) using ultraintense laser pulses in dielectric media has a wide spectrum of applications, ranging from remote sensing to terahertz generation to lightning control. So far, laser filamentation has been triggered with the use of ultrafast pulses with axially symmetric spatial beam profiles, thereby generating straight filaments. We report the experimental observation of curved plasma channels generated in air using femtosecond Airy beams. In this unusual propagation regime, the tightly confined main intensity feature of the axially nonsymmetric laser beam propagates along a bent trajectory, leaving a curved plasma channel behind. Secondary channels bifurcate from the primary bent channel at several locations along the beam path. The broadband radiation emanating from different longitudinal sections of the curved filament propagates along angularly resolved trajectories.

The initial observation of plasma channel generation by intense femtosecond laser pulses in air (*1*) paved the way for a series of fundamental studies in the field of extreme nonlinear optics of gaseous media. Continued interest in the subject is fueled by various potential applications such as remote spectroscopy (*2*), generation of terahertz waves (*3*, *4*), compression of ultrashort laser pulses down to few optical cycles (*5*), and atmospheric science (*6*).

During propagation of an ultraintense and ultrashort laser pulse in a transparent gaseous medium, the defocusing effect of the plasma generated via multiphoton ionization prevents the beam from the self-focusing collapse to a singularity. The hot core of the beam, composed of the high-intensity laser field and the generated plasma, is referred to as the filament. Filaments are typically ~100 μm in diameter and exhibit self-guided, subdiffractive propagation over long distances (*7*–*9*).

One of the important attributes of laser-induced filaments is the forward emission of broadband light, the very property that enables various remote-spectroscopy applications (*2*). This so-called conical emission carries information concerning pulse dynamics, which can be deduced by analyzing the associated angularly resolved spectra in the far field (*10*).

In early studies of femtosecond laser filamentation initiated by ultrashort pulses with Gaussian (*1*) or flat-top (*11*) spatial beam profiles or more complex waveforms such as Bessel (*12*, *13*) and hollow ring beams (*14*), the beams were axially symmetric. Consequently, the plasma channels were always generated along straight lines. Analysis of the conical radiation emanating from straight filaments is complicated by the fact that emissions originating from different longitudinal sections of the beam overlap in the observation plane.

In this study, we used femtosecond pulses with the transverse spatial beam profile in the form of a two-dimensional (2D) Airy function, the so-called Airy beams (*15*, *16*), for the initiation of filamentation. Generation of Airy beams relies on the fact that the Airy function $\mathrm{Ai}(x/x_0)$ and the complex exponential $\exp[i(\beta K)^3/3]$ form a Fourier transform pair, where x and K are conjugate variables and x_0 and β are appropriate scale factors. Thus a plane wave can be converted into an Airy beam by applying a cubic phase modulation followed by a spatial Fourier transformation through focusing with a lens (*15*). Airy beams are not axially symmetric and exhibit the following two unusual characteristics: (i) They remain approximately diffraction-free. (ii) Their main intensity features tend to freely self-bend (or transversely accelerate) during propagation (*15*–*18*). In fact, these beams follow parabolic trajectories in a way analogous to the ballistics of projectiles moving under the action of gravity (*17*). On the other hand, the "center of gravity" of an Airy beam moves along a straight path, in agreement with Ehrenfest's momentum theorem (*17*, *19*). In principle, Airy wave packets can be synthesized simultaneously in both space and time resulting in nondispersive and spatially localized temporal waves or optical bullets that are impervious to both dispersion and diffraction (*16*, *20*).

When intense femtosecond Airy beams are used for initiation of the filamentation, an unusual propagation regime results, in which the binding strength between the filamented beam core and its remaining quasi-linear part can be manipulated by varying the transverse acceleration of the Airy pattern. The generated plasma channel is curved,

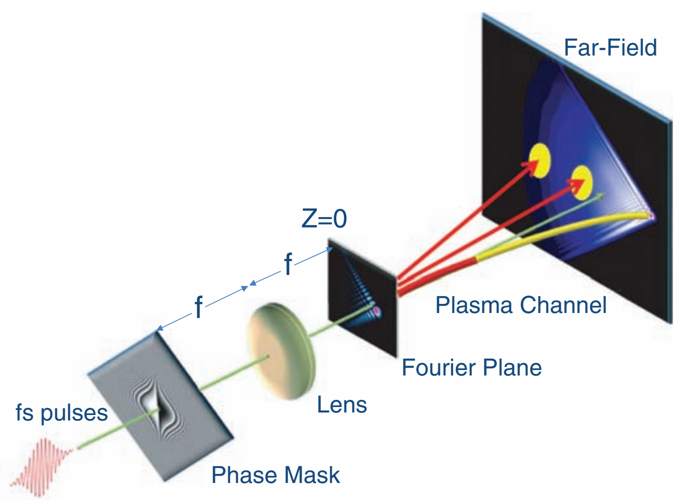

Fig. 1. Experimental setup. The continuous wave visible laser beam that we used as a spatial reference has a much smaller size than that of the phase mask. The reference beam experiences a negligible wavefront modulation and propagates along a straight line.

[1]College of Optical Sciences, University of Arizona, Tucson, AZ 85721, USA. [2]Department of Mathematics, University of Arizona, Tucson, AZ 85721, USA. [3]Center for Research and Education in Optics and Lasers–College of Optics and Photonics, University of Central Florida, Orlando, FL 32816, USA.

*To whom correspondence should be addressed. E-mail: ppolynkin@optics.arizona.edu